High-Performance Sound Detection of Nanoscale-Thick and Large-Area Graphene Oxide Films in Liquids

Shuchao Wang,* Ali K. Yetisen, Martin Jakobi, Quan Zhou,* and Alexander W. Koch

This article presents nanoscale-thick and large-area graphene oxide (GO) films manufactured by a facile method to enable high-performance sound detection in liquids. A Fabry–Perot (F–P) cavity consisting of a GO film, whose vibration diameter is ≈4.4 mm, and a single-mode fiber (SMF) is used as the sensing core for sound detection in liquids. A sound-transparent cap, consisting of a support sleeve and a sound-transparent sleeve, is used to protect the GO-sensing diaphragm to resist liquid pressure to enable long-term stability. The sensing probes with GO diaphragms of ≈100 and 200 nm thickness are placed in ultra-pure water for performance testing. Test results show that they maintain a linear sound pressure response, a flat frequency response, and a uniform directional response from 1 to 100 kHz. They have sensitivities of ≈630 mV Pa^{-1} and about 84 mV Pa^{-1}, respectively, in the range of 1–100 kHz in all directions in different liquids. These results demonstrate the suitability of the nanoscale-thick and large-area GO films for sound detection in liquids with high performance.

1. Introduction

Developing optical detection systems with high accuracy, sensitivity, and robustness is highly desirable in emerging technology industries.[1–5] High-performance sound detection in liquids is a crucial focus in sensing technologies.[6–9] These detectors are used in seas or other liquids, such as strong acidic and alkaline solutions and transformer oil, to listen to underwater sounds.[10–12] Currently, conventional piezoelectric sensors are the dominant detection technology for sound detection in liquids, but there are various drawbacks to this type of sensor,[13–15] for example, the piezoelectric sensors based on circuit systems are susceptible to electromagnetic interference;[13] in addition, a lot of piezoelectric materials used as the sensitive components are vulnerable to moisture and are not suitable for being applied to listen to sounds under liquids for the long term, and they need to be used with protection devices;[14] finally, the output current response of piezoelectric sensors is relatively weak, and they need to be used with a charge amplifier or a high-output impedance circuit.[15] However, photonic sensing systems based on optical fibers and fiber Bragg gratings are well placed to overcome these drawbacks.[16–18] Among many optical detection technologies, extrinsic fiber-optic Fabry–Perot (F–P) sound sensors are advantageous as they offer simple construction, robustness, and low production costs.[19–22]

The core detection component of extrinsic fiber-optic F–P sensors is a sensing diaphragm at the front end of the sensing probe.[23–25] In previous studies,[23–27] different types of elastic materials have been used as sensing diaphragms, such as polymers, metals, silicon, and 2D materials represented by graphene and graphene oxide (GO). These studies showed that the sensitivity of sensing diaphragms is related to the thickness and vibration radius of diaphragms, as well as Poisson's ratio and Young's modulus of diaphragm materials. For diaphragms prepared by a defined material, the thinner the diaphragm thickness and the longer the vibration radius of the diaphragm, the more likely it is that sound detection can be more sensitive. Compared to other materials, the 2D material thickness can be prepared at different nanoscale levels,[28–30] but the application of nanoscale-thick and large-area diaphragms made of 2D materials has been almost unexplored for sound detection in liquids because they are so thin and fragile that it is difficult to resist the liquid pressure.[31]

Here, GO was utilized to prepare sensing films due to its advantages, such as nonconductivity, film-forming ability, excellent adhesion, and high mechanical strength.[32,33] A sound-transparent polyurethane sleeve supported by a 3D-printed stainless steel sleeve has been used to withstand liquid pressure; hence, the GO film can work stably for a long time.

S. Wang, M. Jakobi, A. W. Koch
Institute for Measurement Systems and Sensor Technology
Department of Electrical and Computer Engineering
School of Computation, Information and Technology
Technical University of Munich
80333 Munich, Germany
E-mail: shuchao.wang@tum.de

A. K. Yetisen
Department of Chemical Engineering
Imperial College London
London SW7 2AZ, UK

Q. Zhou
State Key Laboratory of Transmission & Distribution Equipment and Power System Safety and New Technology
School of Electrical Engineering
Chongqing University
Chongqing 400044, China
E-mail: cqzhouquan@cqu.edu.cn

The ORCID identification number(s) for the author(s) of this article can be found under https://doi.org/10.1002/adem.202300962.

Polyurethane elastomers can show sound transmission and absorption properties, mainly determined by the preparation formulation.[34–36] In this work, the sound-transparent sleeve was made of a polyurethane elastomer with sound transmission to form a sound-transparent cap with the 3D-printed stainless steel sleeve together. We have used a simple method to prepare nanoscale-thick and large-area GO films and provided a preliminary regulation analysis, which allowed the construction of the sensing probes. This method provided a fitted mathematical expression for the thickness of GO films as a function of the concentration of GO dispersions and summarized a time-saving, efficient, and thickness-controlled process for the preparation of GO films via liquid precipitation. An F–P cavity consisting of a GO film, whose vibration diameter was ≈4.4 mm, and a single-mode fiber (SMF) was used as the sensing core for sound detection in liquids. It was mainly placed in ultrapure water for performance testing. Test results indicated that nanoscale-thick and large-area GO diaphragms could achieve high-performance sound detection in liquids, which provides possibilities for the rapid development of sensors used for high-performance sound detection in different liquids.

## 2. Production of GO Films and Sensing Probes

Part A of **Figure 1** shows the manufacturing process of GO films with a copper foil. First, GO powder is dissolved in ultrapure water with a resistance higher than 18.5 MΩ by the ultrasonic water bath and magnetic stirring method, resulting in a GO dispersion. Second, as shown in step (1) of Figure 1, GO dispersion

(0.25 mL) is dropped onto the surface of a 10 μm-thick copper foil. The copper foil is placed on a spin-coating machine to resist the surface tension of the GO dispersion droplet and render the prepared GO films more uniform in the process of natural drying, as shown in part A in Figure 1 (step (2) of Figure 1).

Figure 2a shows the surface image of a GO film with a copper foil after step (2) of Figure 1 under a scanning electron microscope (SEM). Figure 2a illustrates that the prepared GO film surface can be considered to be quite flat at a macroscopic scale and has no evident defects (Roughness: 4.777 nm), which were quite important for the production of the sensing probe because the F–P cavity is an optical interference cavity, and it requires that the two surfaces forming the F–P cavity be as flat as possible,[23–25] whereas this surface of the GO film can eventually become one of two flat surfaces forming an F–P cavity in the subsequent manufacturing process. It can be seen from steps (1) and (2) of Figure 1 that the preparation method for GO films is facile and controllable for most beginners. We prepared 20 different thick GO films using GO dispersions with concentrations of 40, 80, 120, 160, 200, 240, 280, 320, 360, 400, 440, 480, 520, 560, 600, 640, 680, 720, 760, and 800 mg L^{-1}, respectively. Figure 2b–d shows the thickness images of GO films prepared by GO dispersions with concentrations of 440, 520, and 600 mg L^{-1} under SEM. Figure 2b–d shows that the average thickness values of GO films prepared by GO dispersion with a concentration of 440, 520, and 600 mg L^{-1} are 299.43, 348.13, and 401.63 nm, respectively. We first took 20 points uniformly on the cross section of a film and measured the width of the cross section at these 20 points, and then calculated the average of these 20 values, which can be used as the representative
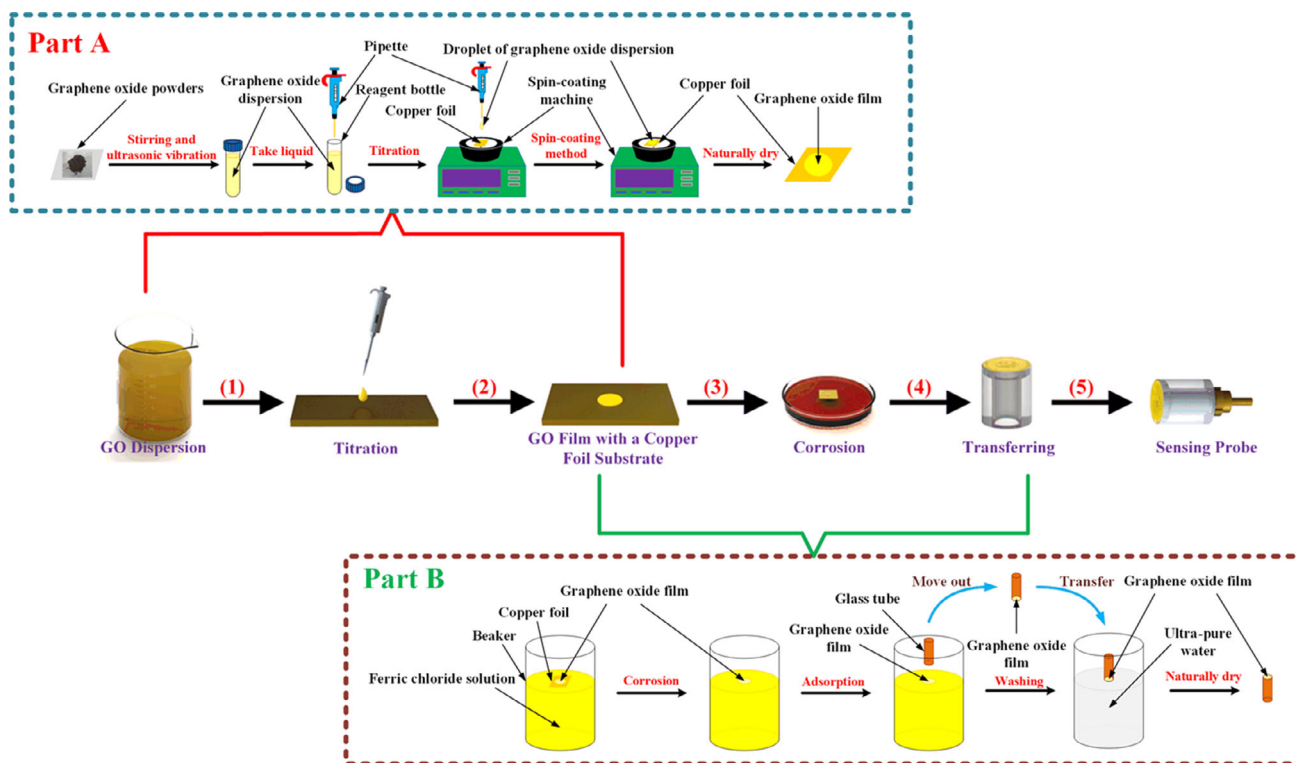
Figure 1. The manufacturing process of GO films and sensing probes.
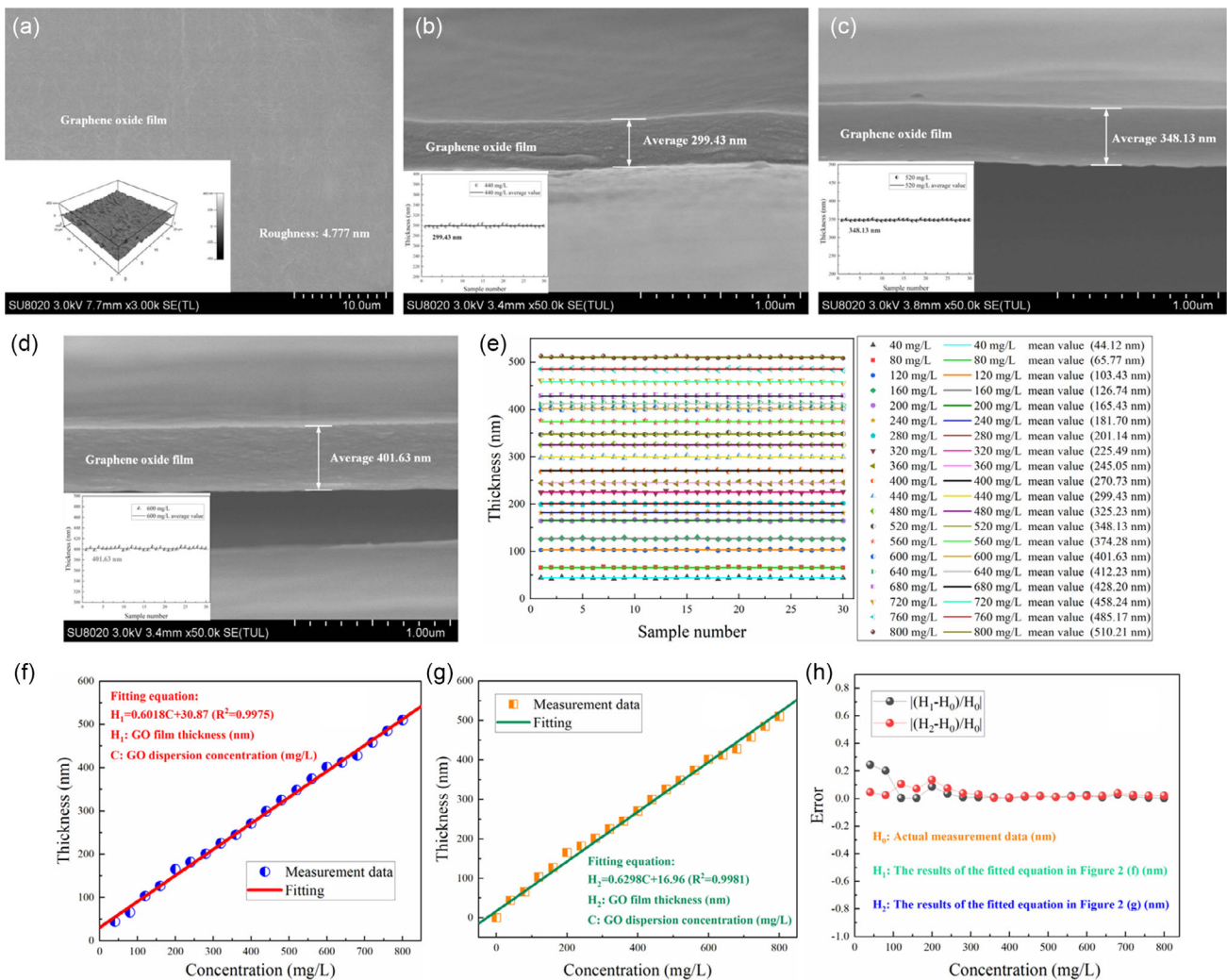
Figure 2. a) SEM image of a GO film surface. SEM image of a GO film thickness prepared by the GO dispersion at a concentration of b) 440 mg L^{-1}, c) 520 mg L^{-1}, and d) 600 mg L^{-1}. e) Representative thickness values of GO films prepared by GO dispersions with 20 different concentrations. f) The fitting equation for these 20 different representative thickness values with no consideration of the zero point. g) The fitting equation for these 20 different representative thickness values when considering the zero point. h) Errors of Equation (1) and (2).

thickness of the GO film. Then, another 29 GO films with the same concentration were taken and the representative thickness values for each of the 29 GO films were measured. Subsequently, the average of the representative thickness values of these 30 GO films was calculated and this value represents the thickness of the GO film at this concentration. Therefore, the average thickness values of GO films at concentrations of 440, 520, and 600 mg L^{-1} in Figure 2b–d are essentially the representative thickness values of GO films at concentrations of 440, 520, and 600 mg L^{-1}. It can be seen from Figure 2b–d that GO film thickness is determined by the concentration of GO dispersion in the preparation method of GO films shown in Part A of Figure 1. Figure 2e shows the representative thickness values of GO films prepared by GO dispersions with concentrations of 40, 80, 120, 160, 200, 240, 280, 320, 360, 400, 440, 480, 520, 560, 600, 640, 680, 720, 760, and 800 mg L^{-1}, respectively.

As shown in Figure 2f, the fitting equation for these 20 different representative thickness values with no consideration of the zero point is

$$H_1 = 0.6018\,C + 30.87 \tag{1}$$

In Equation (1), C represents the GO dispersion concentration; H_1 indicates the GO film thickness, and R^2 is 0.9975.

As shown in Figure 2g, the fitting equation for these 20 different representative thickness values when considering the zero point is

$$H_2 = 0.6298\,C + 16.96 \tag{2}$$

In Equation (2), C represents the GO dispersion concentration; H_2 indicates the GO film thickness, and R^2 is 0.9981.

The errors (Calculation: $|(H_{fitting} - H_{actual})/H_{actual}|$) between the fit GO film thickness values obtained by the Equations (1) and (2) when the GO dispersion concentrations are 40, 80, 120, 160, 200, 240, 280, 320, 360, 400, 440, 480, 520, 560, 600, 640, 680, 720, 760, and 800 mg L^{-1}, respectively, and the actual representative thickness values are shown in Figure 2h. It can be seen from Figure 2h that the error in Equation (1) is lower in the range of 80 to 320 mg L^{-1}. Therefore, the error of Equation (1) is lower for the representative thickness values of GO films in the range of 65.77 to 225.49 nm.

Based on this calculation of Equation (1), the GO dispersions for the preparation of GO films with representative thickness values of 100 and 200 nm should be prepared at concentrations of ≈115 and 281 mg L^{-1}, respectively. As shown in **Figure 3**a, the

representative thickness values of GO films prepared by the GO dispersion with concentrations of ≈115 and 281 mg L^{-1} are ≈100 and 200 nm, respectively. The prepared GO films with a thickness of ≈100 nm have been placed on the surface of a ferric chloride (FeCl$_3$) solution, which corresponds to step (3) of Figure 1. Unsupported GO films can be obtained after copper foil substrates are completely dissolved by FeCl$_3$ solution (Figure 3b). Step (4) of Figure 1 shows the transfer operation of a GO film to the end face of a quartz tube. A quartz tube is used to adhere to a GO film floating on the surface of FeCl$_3$ solution (Figure 3c). The GO film can be adsorbed on the surface of a quartz tube due to the Van der Waals forces.[28–30] Then, the GO film on a quartz tube is immersed in ultra-pure water several times to remove the FeCl$_3$ solution on the surface
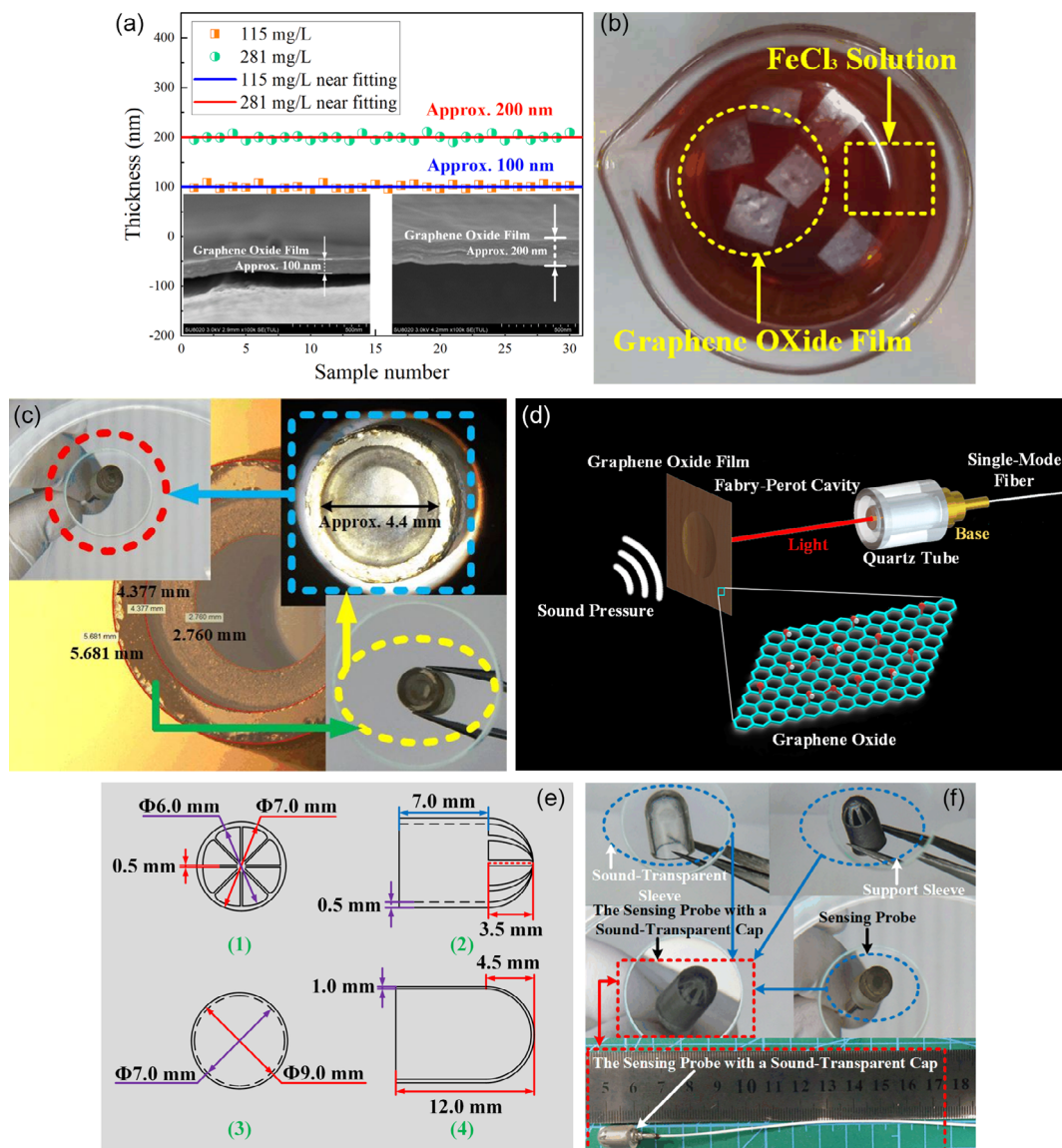
Figure 3. a) Near-fitting thickness values of GO films with two different concentrations of GO dispersions. b) GO films floating on the surface of FeCl$_3$ solution. c) A GO film transferred to the end face of a quartz tube and a sensing probe. d) Sensing principle of extrinsic fiber-optic F–P sound sensors. e) Structures and sizes of the designed support sleeve and sound-transparent sleeve. f) Actual size and shape of the sensing probe with a sound-transparent cap.

of the GO film. The quartz tube with the GO film is left until this GO film is completely dry, thereby achieving the transferring process shown in step (4) of Figure 1. This process is shown in Part B of Figure 1 in detail. Finally, a GO-sensing diaphragm with a thickness and a vibration diameter of about 100 nm and ≈4.4 mm, respectively, can be obtained, as shown in Figure 3c. Compared to previous studies,[19–30] the area of this GO-sensing diaphragm with a vibration diameter of ≈4.4 mm is larger.

To obtain the sensing probe shown in Figure 3c, the sensing principle of extrinsic fiber-optic F–P sensors, as shown in Figure 3d, needs to be understood to deduce an appropriate length of the F–P cavity and the incident light wavelength. The incident light emitted by a tunable laser passes through an SMF into the F–P cavity (Figure 3d). A portion of the incident light is reflected at the end face of the SMF, while the other portion of the incident light propagates into the F–P cavity and is reflected at the inner surface of the diaphragm. The reflected light carrying the length information of the F–P cavity enters the SMF again and interferes with the light inside the SMF on the photodetector, thereby forming interference fringes. The length of the F–P cavity can change when sound pressure causes the diaphragm to vibrate, resulting in a shift of the interference fringes. Therefore, detecting sound signals can be achieved by measuring the phase or intensity change of the interfering light.

The sensing principle can be quantitatively expressed by a relationship between the intensity of the interference light and the length of the F–P cavity.[30] As the end face reflectance of the SMF and the surface reflectance of the GO diaphragm are both less than 50%[30–33] the relationship between the intensity of the interference light and the length of the F–P cavity can be presented as Equation (3).[30]

$$I_R(\lambda, l) = 2\sqrt{r_1 r_2}\left(1 - \cos\left(\frac{4\pi n_0 l}{\lambda}\right)\right)I_0 \tag{3}$$

In Equation (3), $I_R(\lambda, l)$ represents the intensity of the interference light; I_0 indicates the incident light intensity; r_1 is the end face reflectance of the SMF; r_2 represents the surface reflectance of the GO diaphragm; n_0 indicates the refractive index of air in the F–P cavity, generally considered as 1.0;[28–30] λ is the incident light wavelength; l represents the length of the F–P cavity.

Theoretically, as shown in Equation (4), the sensitivity S of the sensing probe can be expressed as the ratio of the intensity of the interference light $I_R(\lambda, l)$ to the length of the F–P cavity l.

$$S = \frac{dI_R(\lambda, l)}{dl} \tag{4}$$

The static working point position can affect the sensing probe sensitivity. The sensitivity S is maximum only when the static working point is at the position of the optimal working point.[22–30] Therefore

$$\frac{d^2 I_R(\lambda, l)}{dl^2} = 0 \tag{5}$$

At this time, the sensor output has only a very small distortion.[30]

According to the deduction of Equation (5), the length l of the F–P cavity can be presented as Equation (6).

$$l = \lambda\left(\frac{2\eta + 1}{8}\right) (\eta \text{ is a positive integer}) \tag{6}$$

It can be seen from Equation (6) that an infinite number of F–P cavity lengths meet the requirement that a static working point is at the position of the optimal working point. However, the environmental temperature can cause a change in F–P cavity length due to thermal expansion and contraction,[28–30] which can cause the static working point to drift. Therefore, the incident light wavelength needs to be adjusted to stabilize the static working point at the position of the optimal working point. However, the F–P cavity length can lead to an excessive free spectral range (FSR) of this sensing probe,[29,30] impeding the stabilization of the static working point at the position of the optimal working point by tuning the incident light wavelength.[30]

Therefore, FSR should be less than or equal to the adjustment range of the incident light wavelength,[30] namely

$$\kappa \cdot FSR \leq \lambda_m - \lambda_n \tag{7}$$

and

$$FSR = \frac{\lambda_a^2}{2l} \tag{8}$$

Therefore

$$l \geq \frac{\kappa \lambda_a^2}{2(\lambda_m - \lambda_n)} \tag{9}$$

In Equation (7)–(9), λ_m represents the maximum incident light wavelength; λ_n indicates the minimum incident light wavelength; λ_a shows the average incident light wavelength; κ is a redundancy factor, generally considered as 1.5.[30]

Furthermore, the length range of the F–P cavity can be calculated from Equation (9) as $l \geq 44.815\,\mu m$, because the wavelength adjustment range of the used tunable laser is 1525–1565 nm.

Theoretically, the longer the F–P cavity length, the more severe the transmission loss of light incident into the F–P cavity.[24–30] Additionally, the adjustment accuracy of a typical translation stage, whose function is to insert an SMF with a ceramic ferrule into a quartz tube to produce the sensing probe, is 0.5 μm.[30] Based on these perspectives, 45 μm has been chosen as the F–P cavity length of the sensing probe.

According to Equation (6), the inequality can be shown as

$$1525\,nm \leq \frac{8l}{2\eta + 1} \leq 1565\,nm \tag{10}$$

Therefore, when $l = 45\,\mu m$, the range of η is approximately 114.5-117.5. Since η is a positive integer, η can be 114-117. When $\eta = 116$, the incident light wavelength is approximately 1545.06 nm, which can allow for the maximum application for the tuning range of a tunable laser because 1545.06 nm is in the center of the tuning range of the used tunable laser (1525–1565 nm). Therefore, the incident light wavelength has been chosen as 1545.06 nm.

**ADVANCED
SCIENCE NEWS**

www.advancedsciencenews.com

**ADVANCED
ENGINEERING
MATERIALS**

www.aem-journal.com

Then the translation stage was used to insert an SMF with a ceramic ferrule with a diameter of 2.5 mm into the quartz tube with a GO film because Figure 3c shows that the minimum inner diameter of the quartz tube is 2.760 mm. The length of the F–P cavity consisting of a GO film and the end face of the SMF was adjusted to ≈45 μm. UV adhesive was used to glue the quartz tube and the ceramic ferrule together to obtain the sensing probe (Figure 3c).

For the sensing probe to be used in liquids, a support sleeve and a sound-transparent sleeve must be designed and manufactured to resist liquid pressure for long-term stability. The schematics (1) and (2) in Figure 3e show the front view and side view of the support sleeve with dimensions. According to the designed structure and the size of each part, the support sleeve shown in Figure 3f has been manufactured with a stainless steel material using 3D printing. The schematics (3) and (4) in Figure 3e show the front view and side view of the sound-transparent sleeve with dimensions. According to the designed structure and the size of each part, this sound-transparent sleeve shown in Figure 3f has been fabricated with a polyurethane elastomer using molding. Then the sensing probe, the support sleeve, and the sound-transparent sleeve were assembled and fixed with UV adhesive, thereby producing the sensing probe with a sound-transparent cap (Figure 3f).

The same manufacturing method was used to fabricate another sensing probe with a GO film with a thickness and vibration diameter of ≈200 nm and about 4.4 mm, respectively.

3. Results and Discussion

A test platform has been built for the performance testing of both sensing probes (**Figure 4**). The liquid environment is simulated by ultrapure water. This platform consisted of a sensing system, an excitation system, and a reference system. The sensing system comprises a tunable laser, an oscilloscope, a circulator, a photodetector, SMFs, and a sensing probe. The excitation system had a sound generator and a signal amplifier with a piezoelectric transducer. The reference system consisted of a reference sensor (Sensitivity: $5.0\,mV\,Pa^{-1}$) with a sound-transparent cap consisting of a support sleeve and a sound-transparent sleeve with the

same thickness and material as that of the proposed sensing probes, a data acquisition card, and a computer with data processing software. The sensing probe, reference sensor, and piezoelectric transducer were placed together in a beaker filled with ultrapure water. In addition, the sensing probe and the reference sensor are placed axisymmetrically. The piezoelectric transducer was placed on the symmetry axis between the sensing probe and the reference sensor, whose purpose was that sound signals generated by the excitation system could act on the sensing probe and the reference sensor simultaneously in the process of performance testing. The ambient environment and ultrapure water temperature were kept at room temperature (25 °C) during the experiment.
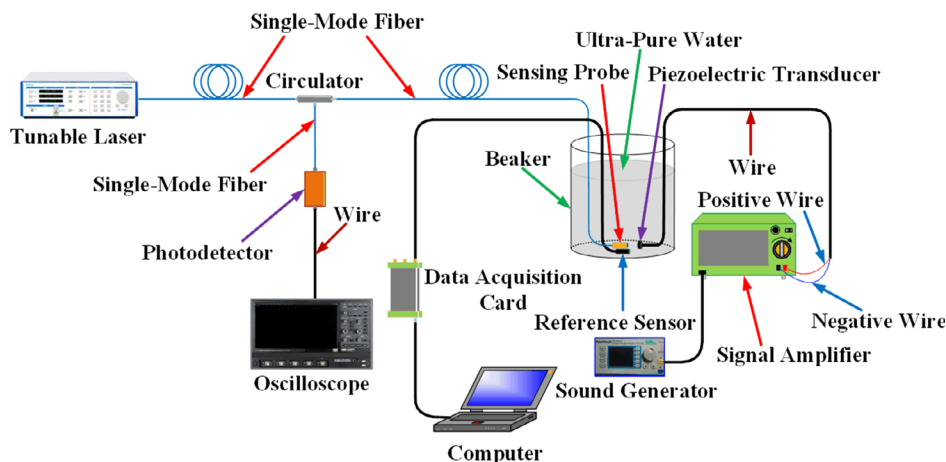
Both sensing probes with GO film thicknesses of ≈100 and 200 nm have been submerged in ultrapure water for performance testing. **Figure 5**a illustrates that the filtered output results in the time domain of both sensing probes and the reference sensor can be obtained when the excitation system produces a sinusoidal sound signal with a frequency of 1 kHz. Figure 5b shows the filtered output results in the frequency domain of both sensing probes under this circumstance. The output voltage amplitudes of both sensing probes were 1859.64 and 240.75 mV, respectively (Figure 5b). As the reference sensor's sensitivity was known ($5.0\,mV\,Pa^{-1}$), the sound pressure acting on both sensing probes can be calculated. Thus, according to this method, both sensing probes have been used to detect sound signals with different intensities at 1 kHz. The output results are shown in Figure 5c.

As shown in Figure 5c, the fitting equation for the relationship between the output voltage amplitude of the sensing probe with a GO film thickness of ≈100 nm and the sound pressure acting on it is
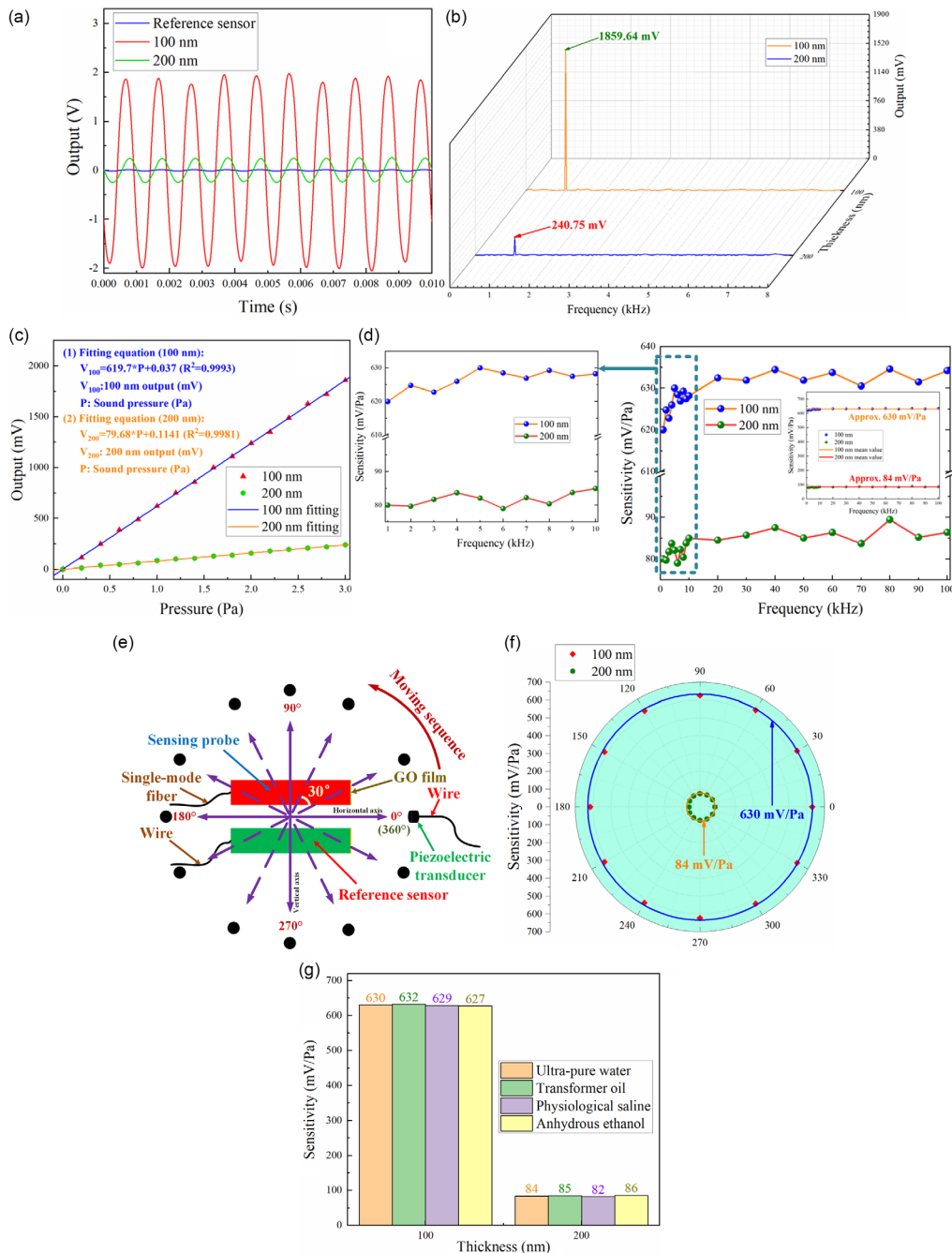
$$V_{100} = 619.7\,P + 0.037 \tag{11}$$

In Equation (11), V_{100} represents the output voltage amplitude of this sensing probe with a GO film thickness of about 100 nm; P indicates the sound pressure acting on the sensing probe, and R^2 is 0.9993.

Similarly, the fitting equation for the relationship between the output voltage amplitude of the sensing probe with a GO film thickness of ≈200 nm and the sound pressure acting on it is

Figure 4. The platform for performance testing of both sensing probes.

**ADVANCED
SCIENCE NEWS**

www.advancedsciencenews.com

**ADVANCED
ENGINEERING
MATERIALS**

www.aem-journal.com

Figure 5. a) Filtered output results in the time domain of both sensing probes and the reference sensor at 1 kHz. b) Filtered output results in the frequency domain of both sensing probes at 1 kHz. c) Sound pressure response characteristics of both sensing probes at 1 kHz. d) Frequency response characteristics of both sensing probes in the range of 1–100 kHz. e) The testing process for the directional response of both sensing probes. f) Directional response characteristics of both sensing probes in the range of 1–100 kHz. g) Sensitivities of both sensing probes in the range of 1–100 kHz in all directions in different liquids.

$$V_{200} = 79.68\,P + 0.1141 \tag{12}$$

In Equation (12), V_{200} represents the output voltage amplitude of the sensing probe with a GO film thickness of about 200 nm; P indicates the sound pressure acting on the sensing probe, and R^2 is 0.9981.

Equation (11) and (12) show that the output voltage amplitude of both sensing probes can rise linearly as the sound pressure continues to increase, which indicates that both sensing probes have a linear sound pressure response to sound signals at different levels. Their sensitivities are 619.7 and 79.68 mV Pa^{-1}, respectively, at 1 kHz.

The sensitivities of both sensing probes can be obtained when the frequency range of sound signals acting on them is 1–100 kHz (Figure 5d). Figure 5d shows that the output voltage amplitude of both sensing probes has minor fluctuations in the difference between two data points in the range of 1–100 kHz, which indicates that both sensing probes have a quite flat frequency response to sound signals in the range of 1–100 kHz. Figure 5d also illustrates that the mean values of the sensitivities for both sensing probes are approximately 630 mV Pa^{-1} and about 84 mV Pa^{-1}, respectively, in the range of 1–100 kHz.

The directional response characteristics of both sensing probes have been analyzed (Figure 5e). Each sensing probe was rotated counterclockwise from 0° to 360°. Testing of the frequency response of each sensing probe in the range of 1–100 kHz was performed at each 30°, so the mean value of the sensitivity of each sensing probe in this frequency range is shown in Figure 5f.

Figure 5f shows that both sensing probes had an approximately equal sensitivity to sound signals from different directions, which indicated that both sensing probes had a uniform directional response to sound signals from different directions. In addition, the sensitivities of both sensing probes in the range of 1–100 kHz in all directions are ≈630 mV Pa^{-1} and about 84 mV Pa^{-1}, respectively.

Both sensing probes were submerged in three common liquids, transformer oil, physiological saline, and anhydrous ethanol, for performance testing. This also allows the sensitivities of both sensing probes to be determined in the range of 1–100 kHz in all directions in different liquids (Figure 5g). The sensitivities of both sensing probes in the range of 1–100 kHz in all directions in different liquids had negligible fluctuation. Therefore, the two sensitivities can still be considered as about 630 mV Pa^{-1} and ≈84 mV Pa^{-1}, respectively. The results show 126 and 16.8 times greater sensitivities than the reference sensor, respectively.

4. Conclusion

In summary, we presented the high-performance sound detection of nanoscale-thick and large-area GO films in liquids. Nanoscale-thick and large-area GO films have been manufactured using a facile and controllable method. A GO film, whose vibration diameter is about 4.4 mm, and an SMF constitute an F–P cavity, whose length is ≈45 μm, of the sensing probe in the condition of the incident light wavelength of about 1545.06 nm. A sound-transparent cap consisting of a support sleeve made of stainless steel material and a sound-transparent sleeve made of a polyurethane elastomer with sound transmission was placed over a sensing probe to resist liquid pressure; hence, this GO sensing diaphragm can work stably for a long time. Both sensing probes with GO diaphragm thicknesses of ≈100 nm and about 200 nm were submerged in ultrapure water for performance testing. Test results indicate that both sensing probes maintained a linearly sound-pressure response, a flat frequency response, and a uniform directional response in the range of 1 to 100 kHz. In addition, both sensing probes were placed in transformer oil, physiological saline, and anhydrous ethanol for performance testing. The testing results indicated that both sensing probes had sensitivities of ≈630 mV Pa^{-1}

and about 84 mV Pa^{-1}, respectively, in the range of 1–100 kHz in all directions in different liquids. These results show that the nanoscale-thick and large-area GO films can achieve high-performance sound detection in liquids, providing a competitive solution for developing sensors.

5. Experimental Section

GO Powder Preparation: The GO powder for the preparation of GO films was prepared by the Hummer method[30] using the physically prepared monolayer graphene powder (Manufacturer: Tanfeng Graphene Technology Co., Ltd., China). The specific preparation process was as follows. First, 2 g graphite powder was mixed with 1 g NaNO$_3$ and put into 80 mL concentrated H$_2$SO$_4$ under an ice bath, and 8 g KMnO$_4$ was slowly added under vigorous stirring to keep the liquid temperature below 20 °C. Then, the mixed liquid was transferred to a constant temperature water bath at 35 °C and stirred for 2 h. Then, 240 mL ultrapure water was added to the paste brown mixture, and at this time, the mixture would release a lot of heat, so the ultrapure water needed to be added slowly and keep the mixture below 50 °C. After completing the addition of the ultrapure water, 5 mL H$_2$O$_2$ with 30% concentration was added to the mixture, and the mixture gradually turned bright yellow in color; after 2 h of stirring, the mixture was then cleaned and filtered and dried under vacuum to obtain the GO powder for the prepared GO films. The prepared GO powder was tested by X-Ray diffraction (XRD) spectroscopy (Device model: BRUCKER D8 ADVANCE; Manufacturer: Bruker Corporation, Germany). A small amount of the prepared GO powder was taken out and well ground until it was free of any graininess. Then, the GO powder with a mass of at least 0.1 g was taken out and tested for a wide-angle XRD, with a scanning range of 5°–90° at the 2θ angle, a scanning rate of 6°/min, and a scanning step of 0.02. The final XRD spectroscopy was obtained, as shown in Figure S1, Supporting Information. According to the analysis and calculation, the crystallinity of the prepared GO powder was 79.47%, as shown in Figure S2, Supporting Information. The GO powder was then tested by the Fourier-transform infrared (FTIR) spectroscopy (Device model: Nicolet IS10; Manufacturer: Thermo Nicolet Corporation, USA) to understand its functional groups and thus further understand the characteristics of the GO powder. In this process, 10 mg GO powder was taken, ground as much as possible, and dried thoroughly using a UV lamp. Furthermore, KBr was used to compress the powder during the test and FTIR spectroscopy was obtained, as shown in Figure S3, Supporting Information. The analysis of FTIR spectroscopy is shown in Table S1, Supporting Information. It can be summarized from Table S1, Supporting Information, that GO has a lot of hydroxyl groups, which may be caused by hydroxyl or carboxyl groups in GO. In addition, there are also carbonyl groups in the GO, which can be judged as carboxy–carbonyl groups. There are also methyl or methylene groups in the GO, but they may be masked due to the strong peak of hydroxyl groups. Besides, olefins and C—O bonds are also present in the GO. To get a clearer understanding of the characteristics of the prepared GO powder, the GO powder was tested by X-Ray photoelectron spectroscopy (XPS; Device model: PHI 5000 Versaprobe III; Manufacturer: ULVAC-PHI Corporation, Japan). A small amount of the GO powder was taken and thoroughly dried, then fully ground, followed by a narrow sweep of C and O elements by XPS testing, the final results of which are shown in Figure S4, Supporting Information. The XPS analysis of the prepared GO powder is shown in Table S2, Supporting Information.

Details: In the preparation of GO dispersions, the GO powder was first placed in ultrapure water and then stirred for a period using a magnetic stirrer (Device model: HJ-4A; Manufacturer: Ronghua Instruments Manufacturing Co., Ltd., China), followed by water bath ultrasonic shaking for an equal period using an ultrasonic shaker (Device model: KQ-200VDE; Manufacturer: Kunshan Ultrasonic Instruments Co., Ltd., China). The stirring and sonication time increased with the concentration of the GO dispersion.

During the natural drying process of the GO dispersion on a copper foil, the spin-coating machine (Device model: EZ4; Manufacturer: LEBO Science Instruments Co., Ltd., China) needed to be kept rotating to resist the surface tension of the GO dispersion droplet and render the prepared GO films more uniform.

To summarize the mathematical expression between the representative thickness of GO films and the concentration of GO dispersions, an SEM (Device model: SU8020; Manufacturer: HITACHI, Japan) was used to measure the thickness of GO films in a short time, low cost, and large quantities.

The time to get an unsupported GO film was related to the concentration of the $FeCl_3$ solution, the higher the concentration of the $FeCl_3$ solution, the shorter the time to get an unsupported GO film.

According to the calculations in Section 2, the range of the F–P cavity length was $l \geq 44.815 \mu m$. A final length of 45 μm was chosen for the F–P cavity of the proposed sensing probe, because the longer the length of the F–P cavity, the more severe the transmission loss of the light incident into the F–P cavity. Figure S5, Supporting Information, shows the relative interference intensities, which are the reflective interference intensities divided by the intensity of the incident light, with different F–P cavity lengths. As shown in Figure S5, Supporting Information, the F–P cavity length of 45 μm produces the highest interference intensity, which enhances the effect of sound-pressure sensing. This is why the length of all F–P cavities was adjusted to about 45 μm in the experimental measurements.

The sound-transparent sleeve produced by a polyurethane elastomer is the main obstacle to the propagation of sound waves, compared to the support sleeve manufactured by stainless steel, because the support sleeve is not a completely closed structure. The sound-transmission characteristics of the polyurethane elastomer with the same thickness as the sound-transparent sleeve are shown in Table S3, Supporting Information. It can be seen from Table S3, Supporting Information, that the average attenuation constant of sound waves ($0.03 dB cm^{-1}$)[37,38] and average sound impedance ($1.554 g \cdot cm^2 \cdot s^{-1}$)[38] are quite low, which indicates that the fine sound-transmission characteristics of the sound-transparent sleeve.

The performance test platform was built by a tunable laser (The central wavelength of approximately 1550 nm; Device model: AP3350A; Manufacturer: APEX Technologies, France), an oscilloscope (Device model: Wave Runner 6Zi; Manufacturer: Teledyne Lecroy, USA), a circulator, a photodetector (Device model: DET08CFC; Manufacturer: Thorlabs, USA), SMFs, the proposed sensing probes, a sound generator (Frequency range: 0-20 MHz; Device model: FY2300; Manufacturer: Feeltech, China), a signal amplifier with a piezoelectric transducer (Frequency range of the signal amplifier: 0–1 MHz; Resonant frequency of the piezoelectric transducer: 300 kHz; Flat frequency range of the piezoelectric transducer: 1–100 kHz; Device model: ATA-2021 H; Manufacturer: Aigtek, China), a reference sensor (Sensitivity: $5.0 mV Pa^{-1}$; Device model: MPA401; Manufacturer: BSWA TECH, China) with a sound-transparent cap consisting of a support sleeve and a sound-transparent sleeve with the same thickness and material as that of the proposed sensing probes, a data acquisition card, and a computer with data processing software together to enable sound detection in a liquid-filled beaker (Volume: 5000 mL), and the details of the experimental platform construction have been presented in Section 3.

Temperature Influence: The F–P cavity length can change under the temperature influence due to thermal expansion and contraction,[39] thus affecting the experimental results. The degree of thermal expansion and contraction for a material is mainly determined by its average coefficient of thermal expansion, that is, the greater the value, the more severe the material is affected by temperature.[40] The average coefficient of thermal expansion of the quartz tube ($5.0 \times 10^{-7} {}^{\circ}C^{-1}$) was much lower than that of common materials,[40,41] so the F–P cavity length was theoretically affected slightly by temperature. Figure S6, Supporting Information, shows the frequency responses of both proposed sensing probes at different temperatures under the same experimental condition. It can be seen from Figure S6, Supporting Information, that the performance of both proposed sensing probes is slightly influenced by temperature.

Supporting Information

Supporting Information is available from the Wiley Online Library or from the author.

Conflict of Interest

The authors declare no conflict of interest.

Data Availability Statement

The data that support the findings of this study are available from the corresponding author upon reasonable request.

[1] A. G. Leal-Junior, C. Marques, *IEEE Sens. J.* **2021**, *21*, 12719.

[2] B. Vanus, C. Baker, L. Chen, X. Y. Bao, *Opt. Express* **2021**, *29*, 32114.

[3] X. K. Yin, Y. L. Su, T. L. Xi, B. S. Chen, L. Zhang, X. S. Zhang, L. X. Liu, X. P. Shao, *J. Appl. Phys.* **2022**, *131*, 130701.

[4] G. M. Ma, H. Y. Zhou, M. Zhang, C. R. Li, Y. Yin, Y. Y. Wu, *IEEE Sens. J.* **2019**, *19*, 9235.

[5] M. Ren, S. Y. Wang, J. R. Zhou, T. X. Zhuang, S. J. Yang, *Sens. Actuators, A* **2018**, *283*, 113.

[6] H. J. Liu, E. B. Fan, H. X. Xu, Y. H. Wu, Y. He, J. Li, J. Ma, B. O. Guan, *J. Lightwave Technol.* **2022**, *40*, 2523.

[7] N. Wu, S. Haruyama, *Opt. Express* **2020**, *28*, 4475.

[8] J. L. Shi, N. Xu, N. N. Luo, S. J. Li, J. J. Xu, X. D. He, *Opt. Express* **2022**, *30*, 16419.

[9] Z. W. Song, S. Y. Xiang, Z. X. Ren, S. H. Wang, A. J. Wen, Y. Hao, *Opt. Express* **2020**, *28*, 1561.

[10] C. W. Broadman, C. J. Naify, M. J. Lee, M. R. Haberman, *J. Appl. Phys.* **2021**, *129*, 194902.

[11] S. C. Li, J. L. Zheng, J. Yan, Z. J. Wu, Q. Zhou, L. Tan, *ACS Appl. Mater. Interfaces* **2019**, *10*, 42573.

[12] N. X. Jia, T. Wang, J. W. Duan, K. Qing, S. Xia, H. L. Du, F. Li, Z. Xu, *ACS Appl. Mater. Interfaces* **2022**, *14*, 8137.

[13] W. R. Ali, M. Prasad, *Sens. Actuators, A* **2020**, *301*, 111756.

[14] R. C. Turner, P. A. Fuierer, R. E. Newnham, T. R. Shrout, *Appl. Acoust.* **1994**, *41*, 299–.

[15] V. T. Rathod, *Sensors* **2020**, *20*, 4051.

[16] G. Wild, S. Hinckley, *IEEE Sens. J.* **2008**, *8*, 1184.

[17] D. Tosi, C. Molardi, M. Sypabekova, W. Blanc, *IEEE Sens. J.* **2021**, *21*, 12667.

[18] A. Sampaolo, P. Patimisco, M. Giglio, A. Zifarelli, H. P. Wu, L. Dong, V. Spagnolo, *Anal. Chim. Acta* **2022**, *1202*, 338894.

[19] M. R. Islam, M. M. Ali, M. H. Lai, K. S. Lim, H. Ahmad, *Sensors* **2014**, *14*, 7451.

[20] J. W. Meriwether, *J. Atmos. Sol.-Terr. Phys.* **2006**, *68*, 1576.

[21] Z. Li, P. G. Jia, G. C. Fang, H. Liang, T. Liang, W. Y. Liu, J. J. Xiong, *Appl. Opt.* **2018**, *57*, 1738.

[22] X. L. Yin, Y. D. Shen, D. Su, Z. H. Shao, *Opt. Commun.* **2019**, *453*, 124422.

[23] J. Liu, P. G. Jia, H. X. Zhang, X. D. Tian, H. Liang, Y. P. Hong, T. Liang, W. Y. Liu, J. J. Xiong, *Appl. Opt.* **2018**, *57*, 4211.

[24] C. R. Liao, S. Liu, L. Xu, C. Wang, Y. P. Wang, Z. Y. Li, Q. Wang, D. N. Wang, *Opt. Lett.* **2014**, *39*, 2827.

[25] Y. Wang, D. N. Wang, C. Wang, T. Y. Hu, *Opt. Express* **2013**, *21*, 14084.

[26] F. W. Guo, T. Fink, M. Han, L. Koester, J. Turner, J. S. Huang, *Opt. Express* **2012**, *37*, 1505.

[27] L. Liu, P. Lu, S. Wang, X. Fu, Y. Sun, D. M. Liu, J. S. Zhang, H. Xu, Q. P. Yao, *IEEE Photonics J.* **2016**, *8*, 6800709.

[28] F. F. Yu, Q. W. Liu, X. Gan, M. X. Hu, T. Y. Zhang, C. Li, F. Y. Kang, M. Terrones, R. T. Lv, *Adv. Mater.* **2017**, *29*, 1603266.

[29] J. Ma, H. F. Xuan, H. L. Ho, W. Jin, Y. H. Yang, S. C. Fan, *IEEE Photonics Technol. Lett.* **2013**, *25*, 932.

[30] S. C. Wang, W. G. Chen, *Nanomaterials* **2020**, *10*, 2312.

[31] Q. Zhou, J. L. Zheng, S. Onishi, M. F. Crommie, A. K. Zettl, *Proc. Natl. Acad. Sci. USA* **2015**, *112*, 8942

[32] G. Eda, G. Fanchini, M. Chhowalla, *Nat. Nanotechnol.* **2008**, *3*, 270.

[33] D. A. Dikin, S. Stankovich, E. J. Zimney, R. D. Piner, G. H. B. Dommett, G. Evmenenko, S. T. Nguyen, R. S. Ruoff, *Nature* **2007**, *448*, 457.

[34] T. M. Yu, F. C. Jiang, X. Cui, M. X. Cao, C. H. Guo, Z. Q. Wang, Y. P. Chang, *J. Appl. Polym. Sci.* **2020**, *138*, 49891.

[35] Z. J. Zhang, H. Jiang, R. Li, S. Gao, Q. Wang, G. J. Wang, X. Ouyang, H. Wie, *J. Appl. Polym. Sci.* **2020**, *138*, 49970.

[36] H. E. Esen, M. Yagimli, H. Tozan, G. E. Yalcin, E. Arca, *Trans. Inst. Met. Finish.* **2020**, *98*, 271.

[37] S. Bahl, A. K. Bagha, S. Sehgal, *Mater. Today: Proc.* **2021**, *44*, 2048.

[38] S. Malakooti, H. G. Churu, A. Lee, T. G. Xu, H. Y. Luo, N. Xiang, C. Sotiriou-Leventis, N. Leventis, H. B. Lu, *J. Non-Cryst. Solids* **2017**, *476*, 36.

[39] G. K. White, *Contemp. Phys.* **1993**, *34*, 193.

[40] V. A. Shutilov, B. S. Abesgaus, *Vestn. Leningr. Univ., Ser. 4: Fiz., Khim.* **1986**, *3*, 18

[41] I. G. Polyakova, in *Glass: Selected Properties and Crystallization*, De Gruyter, Berlin, Germany **2014**.

2300962 (10 of 10)